Cement & Concrete Composites 33 (2011) 956–965

Contents lists available at SciVerse ScienceDirect

Cement & Concrete Composites

journal homepage: www.elsevier.com/locate/cemconcomp

Tensile fracture process of Strain Hardening Cementitious Composites by means of three-dimensional meso-scale analysis

Minoru Kunieda [a,*], Hiroki Ogura [b], Naoshi Ueda [a], Hikaru Nakamura [a]

[a] Dept. of Civil Engineering, Nagoya University, Nagoya, Japan
[b] Shimizu Institute of Technology, Tokyo, Japan

ARTICLE INFO

Article history:
Received 23 June 2010
Received in revised form 27 May 2011
Accepted 28 May 2011
Available online 12 June 2011

Keywords:
SHCC
Discretized fiber
Rigid-Body-Spring Model (RBSM)
Meso-scale analysis
Uniaxial tensile test
Probability distribution

ABSTRACT

There are a wide variety of short fiber reinforced cement composites. Among these materials are Strain Hardening Cementitious Composites (SHCC) that exhibit strain hardening and multiple cracking in tension. Quantitative material design methods considering the properties of matrix, fiber and their interface should be established. In addition, numerical models to simulate the fracture process including crack width and crack distribution for the material are needed.

This paper introduces a numerical model for three-dimensional analysis of SHCC fracture, in which the salient features of the material meso-scale (i.e. matrix, fibers and their interface) are discretized. The fibers are randomly arranged within the specimen models. Load test simulations are conducted and compared with experimental results. It is seen that the proposed model can well simulate the tensile failure of Ultra High Performance-Strain Hardening Cementitious Composites (UHP-SHCC) including strain-hardening behavior and crack patterns. The effects of matrix strength, its probability distribution inside the specimen and fiber distribution on the tensile fracture are numerically investigated. Consideration of the probability distributions of material properties, such as matrix strength, appears to be essential for predicting the fracture process of SHCC.

1. Introduction

A variety of concepts and design methods have been proposed in recent years to improve the performance of short fiber reinforced cementitious composites. Notable amongst these high-performance materials are Strain Hardening Cementitious Composites (SHCC), such as Engineered Cementitious Composites (ECC) that have been developed using micro mechanics principles [1]. The effects of fiber orientation and heterogeneity due to the fiber distribution on tensile fracture processes cannot be, however, investigated through ordinary material design concepts.

In order to enhance the desirable properties of SHCC, not only global structural response but also characteristics of the fracture process (e.g. crack width, number of cracks and crack spacing) should be appropriately estimated by a numerical approach. Most models of fracture of fiber reinforced cementitious composites are based on either:

(1) stress–strain behavior of homogenized continua;
(2) bridging stress of fibers (and possibly the matrix) versus cracking opening displacement; or
(3) bond stress–slip behavior of fibers at the meso-level.

For the stress–strain based modeling, stress–strain curves obtained from experiments are required for the analysis. The contribution of fibers can be represented by the improved tensile strength and strain capacity. This modeling approach is the easiest and the most straightforward for finite element analysis based on continuum mechanics [2,3].

For the modeling based on bridging stress-crack opening displacement, the composite is commonly modeled as a homogeneous material before initial cracking. After the initial cracking, the responses of the crack and un-cracked part are modeled individually. Traction by fiber bridging during pull-out or rupture of fibers is represented by the bridging stress-crack opening displacement relation, which can also be obtained by experiments [4,5]. In such models, the crack spacing and crack width can be estimated in addition to the improvement of mechanical properties due to fiber bridging.

For the bond stress–slip based modeling, the cement matrix and each fiber in a composite are modeled separately. Especially, the location of each fiber should be identified. Bolander and Saito [6], for instance, conducted 2-D parametric analyses in which short fibers were discretized as beam elements to examine tensile fracture of fiber reinforced concrete, and the effect of the fiber distribution on the mechanical performance of the resulting composite from

* Corresponding author. Address: Dept. of Civil Engineering, Nagoya University, Furo-cho, Chikusa-ku, Nagoya 464-8603, Japan. Tel./fax: +81 52 789 4633.
E-mail address: kunieda@nagoya-u.jp (M. Kunieda).

0958-9465/$ - see front matter © 2011 Elsevier Ltd. All rights reserved.
doi:10.1016/j.cemconcomp.2011.05.010

the viewpoint of cracking patterns. Through this model, materials using hybrid fibers (i.e. combinations of different fiber lengths or fiber types) can also be analyzed. Jun and Mechtcherine [7] developed a model by superimposing the pullout responses of all fibers involved in the crack-bridging action to represent a stress-crack opening relationship for each individual crack including the unloading and reloading parts. Kabele [8] also proposed a constitutive model for PVA-ECC. The proposed model is based on the relation between the overall stress–strain curves and their local counterparts (bridging tractions, crack opening/sliding displacements). The approach with the nominal stress–strain curve cannot, however, provide the information about crack width and crack distribution directly.

This paper presents results of a discrete modeling approach applied to UHP-SHCC; the approach is based on the bond stress–slip modeling of individual short fibers, as previously described. In order to interpret the fracture mechanism (in terms of material strength, strain capacity and crack patterns), parametric analyses are performed in which probability distributions of matrix strength and fiber placement are considered.

2. Outline of proposed model

2.1. Rigid-Body-Spring Model (RBSM)

Fig. 1 shows two polyhedral (Voronoi) cells from which the element stiffness matrix is formed in the 3-D RBSM [9]. Each cell is assumed to be a rigid body and possess six degrees of freedom (defined at the nodal point used to construct the Voronoi cell). Six springs connect neighboring cells across their common facet; each spring set is composed of one facet-normal and two facet-tangential extensional springs and three rotational springs. The properties (tensile strength, elastic modulus, and fracture energy) of the matrix define the mechanical properties of the normal and tangential springs, whereas the properties of the rotational springs are based on the facet geometry [9]. Note that fracture is evaluated using a crack band approach to minimize the effect of the discretization on the cracking properties [10]. The crack band forms between the neighboring nodes and has a maximum width h, which corresponds to the distance between the neighboring nodes.

2.2. Modeling of fiber action before cracking of the cement matrix

Before cracking of the cement matrix, the stress borne by fibers is calculated based on the shear lag theory of Cox [11]. Cox expressed the tensile stress distribution acting in fibers within the matrix as

$$\sigma_f(x) = E_f \varepsilon_m \left\{ \frac{1 - \cosh \beta(l/2 - x)}{\cosh \beta(l/2)} \right\} \quad (1)$$

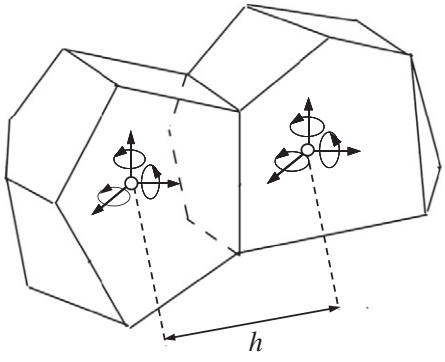

Fig. 1. Rigid cells and defined degrees of freedom.

where $\sigma_f(x)$ = fiber tensile stress (MPa), E_f = fiber elastic modulus (MPa), ε_m = matrix strain, l = embedment length (mm), x = distance from the end of fiber (mm), and β = constant determined by several factors (and set to 1.0 in this study).

2.3. Modeling of fiber action after cracking

2.3.1. Outline of modeling

Short fibers with a given length are randomly arranged in the specimen model, so as to attain the specified fiber content by volume. As shown in Fig. 2, a zero-size spring is placed at each point where a fiber crosses a facet common to two cells, and the fiber bridging force obtained from the integration of bond stress versus slip relationship acts on the spring. The embedment length l and the angle to the facet-normal (orientation angle) ϕ are also calculated for each fiber. Note that the orientation angle can be determined from the inner product of the vector normal to the boundary surface of the element and the vector in the direction of fiber orientation.

After cracking, the stress transfer by fibers across a crack plane in the matrix is calculated by the steps shown in Fig 3 [12]. Half of the calculated crack width is assumed to be the length of fiber pull-out displacement before softening of the bond stress slip relation. After softening, pull-out displacement was assumed to be equal to

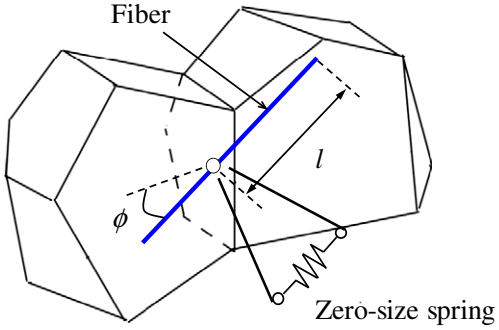

Fig. 2. Fiber location and zero-size spring.

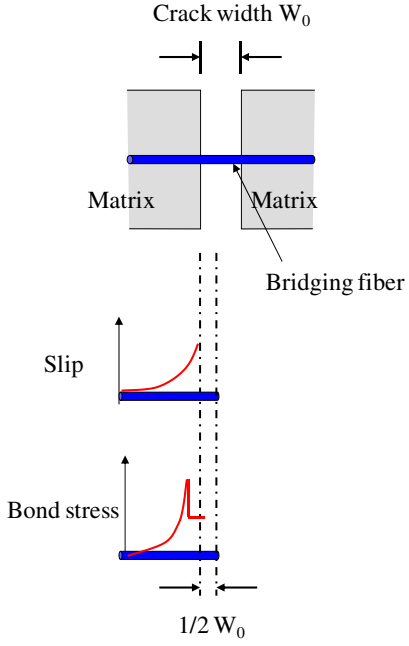

Fig. 3. Relation between pullout displacement and crack width prior to softening of the fiber–matrix composite.

total crack width. The shape of the slip distribution was determined through the analysis of single fiber pull-out tests. If the shape of slip distribution is known, then the bond stress distribution is determined from the bond stress–slip relationship. The bridging forces of fibers across cracks can then be calculated by integrating the bond stress distribution in the direction of the fiber axis. Uniaxial bond stress–slip curve as shown in Fig. 4 was identified through the results of single fiber pull-out tests [13]. Normal force to the crack plane due to crack opening was modeled; traction produced by shear deformation across the crack plane was not considered.

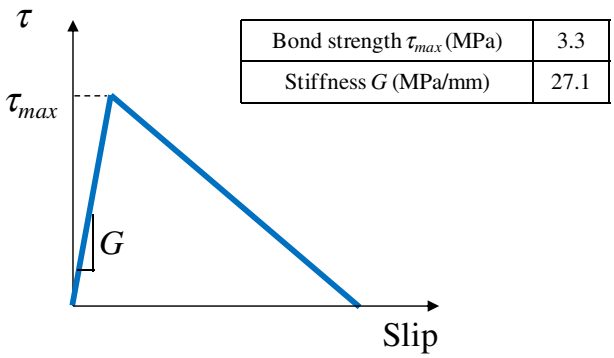

Fig. 4. Bond stress–slip relation (PE fiber, W/B = 0.18).

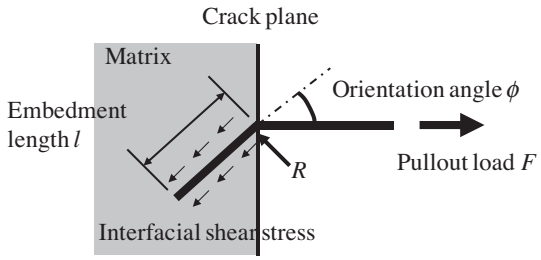

Fig. 5. Bridging of inclined fiber across the crack plane.

2.3.2. Increase of bond strength of inclined fiber

As shown in Fig. 5, fibers are not always oriented perpendicular to crack plane, and that means the fiber has an orientation angle ϕ. Li et al. [14] revealed the increase of bond strength in the inclined fiber pull-out test, and derived the following equation:

$$F = F_0 e^{f\phi} \tag{2}$$

where F = pull-out load (N), ϕ = orientation angle of fiber (rad.), F_0 = pull-out load for $\phi = 0$ (N), f = parameter representing the snubbing effect. Regarding the parameter f, 0.5 was identified through numerical results [15].

2.3.3. Decrease of rupture strength of inclined fiber

It is well known that the strength of inclined fiber itself was decreased due to surface damage during the pull-out process in the case of PVA fiber, and reduced fiber strength was often used in the modeling [16]. On the other hand, it has been experimentally confirmed that the pull-out of fiber was mainly observed in the case of PE fiber because of the ultra high strength. In this study, the apparent fiber strength value was used for the analysis.

2.4. Pull-out behavior of single fiber in proposed model

Tensile specimens with only one embedded fiber are analyzed to verify the model. Fig. 6 shows the geometry of the tensile spec-

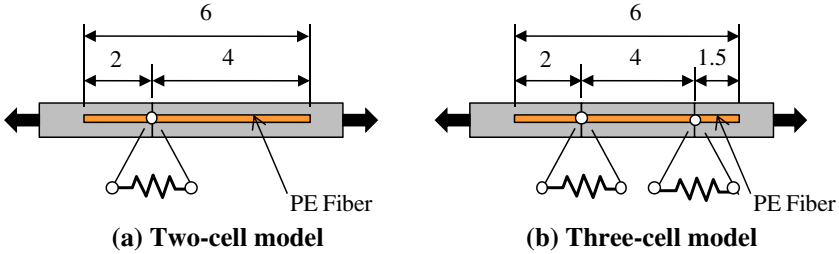

Fig. 6. Tensile specimens with a single embedded fiber (dimensions in mm).

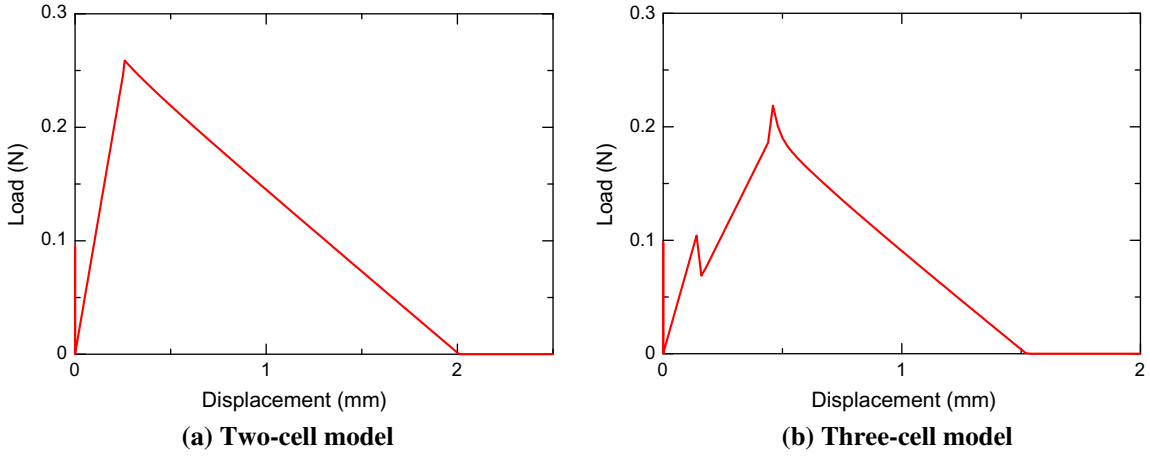

Fig. 7. Load–displacement curves for the fiber–matrix composite.

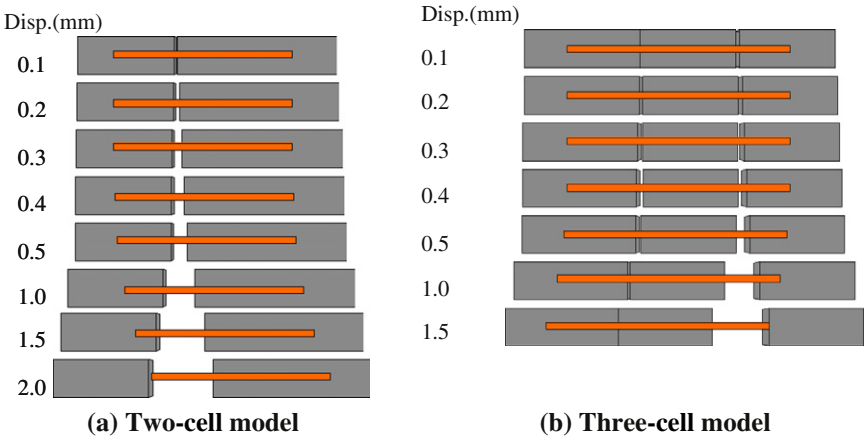

Fig. 8. Pull-out behaviors.

imen with a cross-section of 1 mm × 1 mm. Two discretizations are considered, as shown in Fig. 6. Tensile strength of the matrix is assumed to be small (0.1 MPa), because the maximum fiber bridging force should exceed the cracking load of the matrix to access the cracking behavior of the composite.

Fig. 7 shows the load–displacement curves of each model. In both models, an increase of the load was observed after matrix cracking (at 0.1 N). In the case of the three-cell model, secondary cracking was observed at same load level as the initial cracking load (0.1 N). Since the maximum load in these curves depends on the shortest embedment length of each fiber, the maximum load of the three-cell model was lower than that of two-cell model. The values of displacement at complete pull-out are 2 mm and 1.5 mm for the two- and three-cell models, respectively. These values correspond to the shortest embedment length of the fiber in each respective model, as shown in Fig. 8. As mentioned above, the results from this model depend on the relative positioning of the interface (potential crack plane) and fiber, and are ultimately controlled by the pull-out behavior of the shortest embedment length of each fiber.

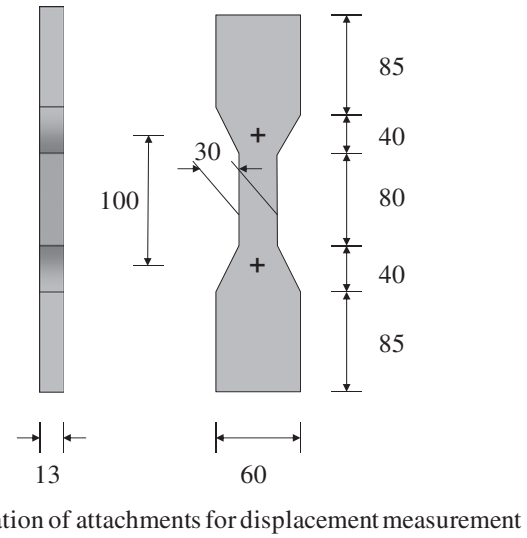

Fig. 9. Dimensions of dumbbell-shaped specimen (in mm).

3. Tensile loading of SHCC specimens

The target of this analysis is Ultra High Performance-Strain Hardening Cementitious Composites (UHP-SHCC) developed by Kunieda et al. [17,18]. In tension, the composite exhibits high strength (>8 MPa) and high strain capacity (>2%), with high durability due to its low water to binder ratio (0.18–0.22). Uniaxial tensile tests of specimens containing 0.5%, 1.0% and 1.5% polyethylene (PE) fibers (6 mm in length and 0.012 mm in diameter) were carried out. Dumbbell-shaped specimens were used in the tests and strain was measured over a 100 mm gage length, as shown in Fig. 9.

The stress–strain curves obtained from the specimens with different fiber contents are shown in Fig. 10. In the case of 0.5% fiber volume fraction, softening behavior was obtained after first cracking; this occurred at a strength equal to only about 4 MPa. In the case of 1.0% fiber volume fraction, slight strain hardening behavior up was obtained to about 1.0% strain, with the repeated stress gains and losses after the first cracking. For the 1.5% fiber volume fraction, a significant strain hardening behavior was obtained, with a large ultimate tensile strain (>2%) and high tensile strength (>9 MPa).

Final crack patterns obtained from each specimen with different fiber content are shown in Fig. 11. The number of cracks increases with increasing fiber content, and the average crack width after the

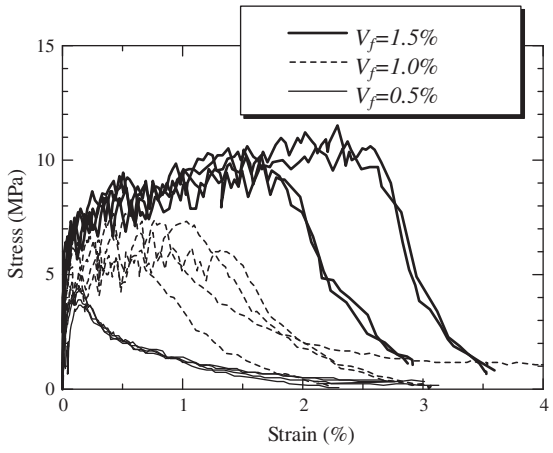

Fig. 10. Tensile stress–strain curves of specimen with different fiber contents.

tensile tests (unloaded) was less than 30 μm in the case of 0.5% fiber volume fraction. For the 1.0% and 1.5% fiber volume fractions, average crack width was less than 10 μm, as observed by a microscope.

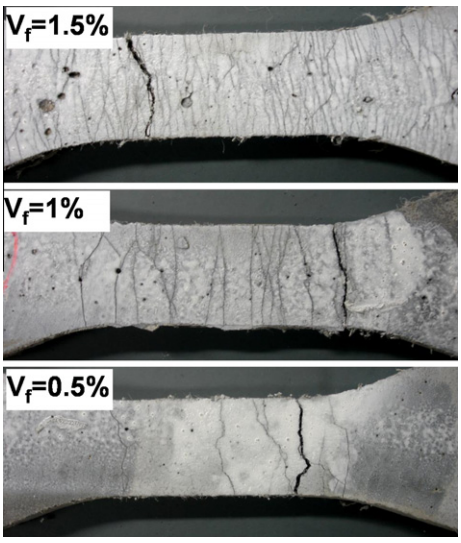

Fig. 11. Final crack patterns after tensile tests.

4. Analysis of SHCC cracking

4.1. Outline of analysis

The 100 mm gage lengths of the specimens considered in the previous section are modeled as shown in Fig. 12. When using the RBSM approach, the onset and propagation of cracks can be strongly affected by the mesh size and shape. For the sake of simplicity and computational efficiency, cells of rectangular (30×13 mm^2) cross-section were used at a spacing of 1 mm in the longitudinal direction of the specimen. This 1 mm spacing of potential crack planes is less than the experimental crack spacing. Fibers were modeled by randomly dispersing them in the specimen as shown in Fig. 12. Displacement controlled loading was applied in the longitudinal direction. Table 1 gives the physical properties of the fibers, matrix, and fiber–matrix interface for the analysis.

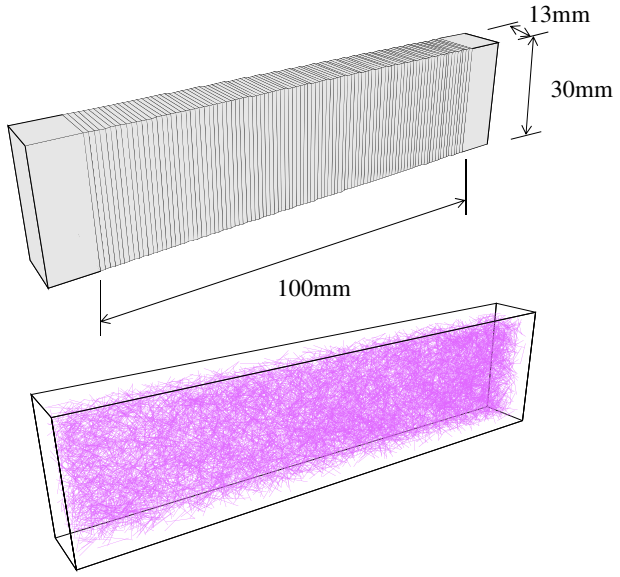

Fig. 12. Discritized cement matrix and fibers (V_f = 0.5%).

Table 1
Material properties for analysis.

Fiber	Length L_f (mm)	6
	Diameter d_f (mm)	0.012
	Elastic modulus E_f (GPa)	88
	Apparent strength σ_{fu}^n (MPa)	2700
	Volume fraction V_f (%)	0.5, 1.0, 1.5
Matrix	Elastic modulus E_m (GPa)	37.8
	Fracture energy G_{ft} (N/m)	20
Interface (bond)	Chemical bond strength τ_s (MPa)	3.3
	Stiffness G (MPa/mm)	27.1

4.2. Trial analysis for specimen with different fiber contents

Fig. 13 compares the stress–strain relationships provided by the model with those of the experiments. The tensile strength used in the analyses (7.5 MPa) was determined through flexural strength testing of the plain (unreinforced) matrix. It was assumed that tensile and flexural strengths were equal.

In the case of 0.5% fiber volume fraction, the initial crack occurred at a stress of 7.5 MPa. After a sudden stress drop, the stress increases to 3 MPa, after which softening behavior was observed. In this case, total response can be well simulated. The model also predicts the softening behavior in the case of 1.0% fiber volume fraction, although the experimental results show slight hardening up to 1.0% strain. With reference to the numerical results for 1.5% fiber volume fraction case, the analysis reproduced the repeated stress gains and losses after the first crack and a large ultimate tensile strain (exceeding 5%, although the test results only showed an ultimate strain capacity ranging from 2.0% to 2.5%). In the modeling, no increase in stress was observed up to a 2.0% strain because of the cracking strength of 7.5 MPa. After that, the model exhibits strain hardening up to a strain of 5.2%. The total response cannot be correctly simulated from a quantitative point of view. Fig. 14 shows the numerically predicted crack patterns at strains equal to 1.0%, 2.0% and 4.0%. In strain hardening materials with multiple fine cracks, the number of cracks strongly affects the strain capacity in tension. As shown in the crack patterns obtained from the analyses, most interfaces between the cells, which correspond to potential crack locations, were opened, and induced nearly constant crack spacing at each strain level.

Although the peak strengths in the experiments were roughly simulated by the numerical analysis, the total response including strain hardening behavior were not simulated quantitatively. One of the reasons is that the actual materials are characterized by a spatial distribution of their properties (i.e. matrix strength and fiber orientation, etc.), which may cause sequential cracking within a specimen. In the following section, parametric studies are conducted that consider the probability distributions of matrix strength and fiber placement within the specimens.

5. Effects of nonuniform distribution of material properties on tensile response

5.1. Effect of matrix strength and its probability distribution

Fig. 15 shows the numerical results with different matrix strength, in the case of 1.5% fiber volume fraction. Three values of matrix strength (5.0 MPa, 7.5 MPa and 10 MPa) were adopted. It is worth remarking that the bond properties in this parametric study were assumed to be constant, although they should be affected by changes in matrix strength. As shown in Fig. 15, as the matrix strength became lower, the strain capacity became higher with strain hardening behavior. Because the fiber bridging strength was equal to about 10 MPa in the case of 1.5% fiber volume fraction, as shown in Fig. 15, matrix strength lower than 10 MPa may cause significant strain hardening behavior.

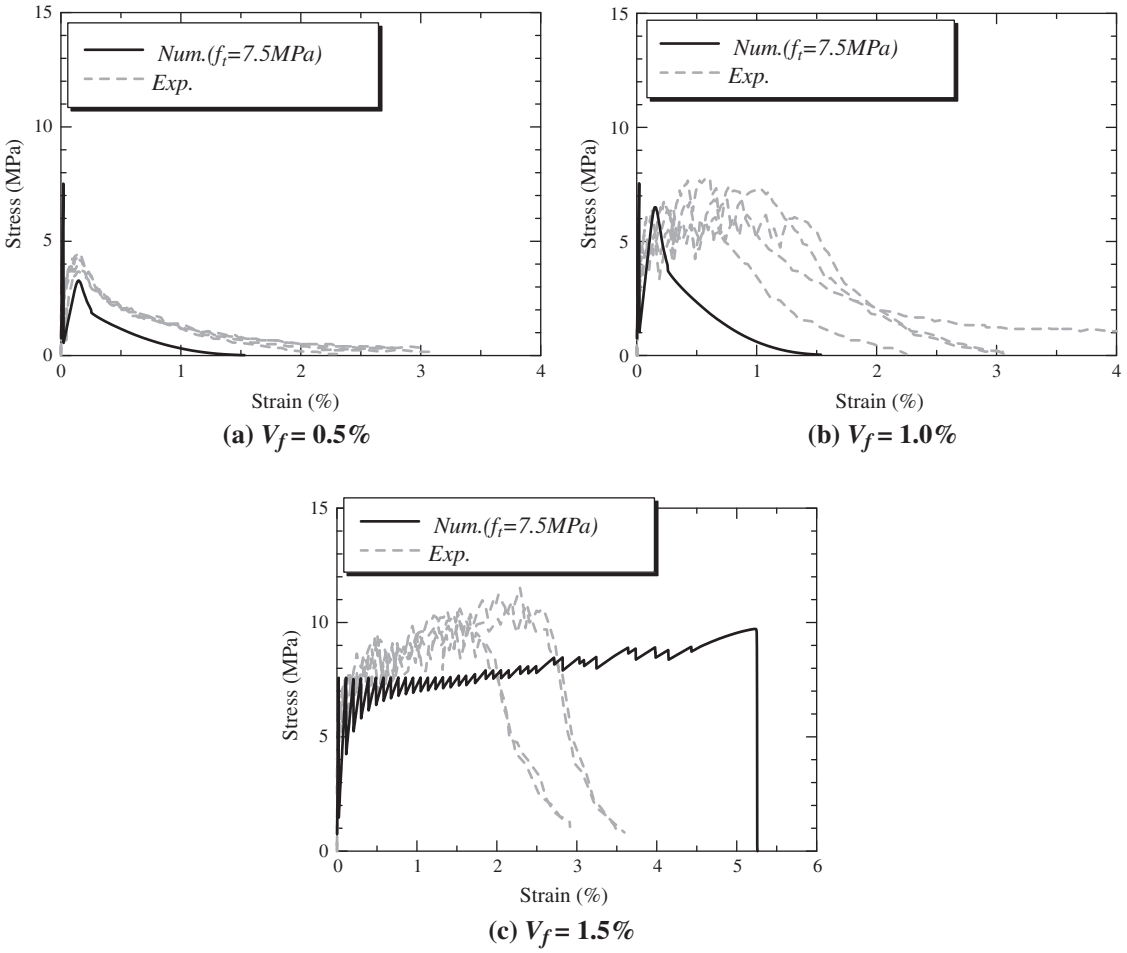

Fig. 13. Stress–strain curves of specimen with different fiber contents.

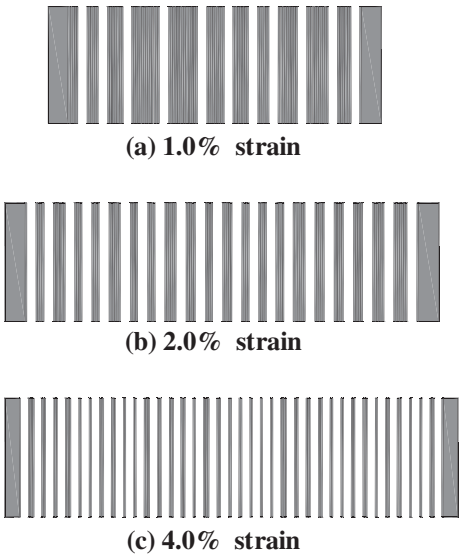

Fig. 14. Crack patterns in numerical analysis (V_f = 1.5%).

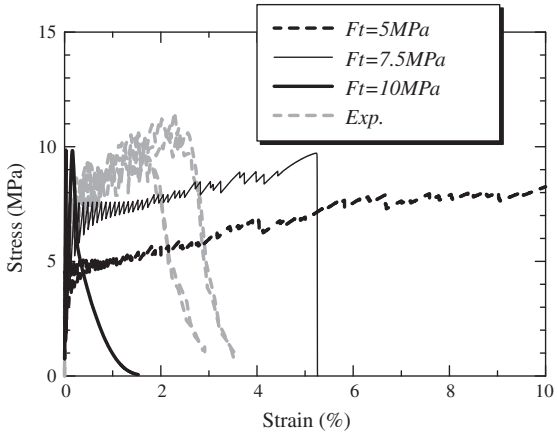

Fig. 15. Effect of matrix strength (V_f = 1.5%).

Fig. 16 shows the numerical results for nonuniform assignments of matrix strength. The matrix strength is assumed to be normally distributed along the specimen axis, and three levels of standard deviation (SD = 0 MPa, 1.0 MPa and 2.0 MPa) were analyzed for an average strength equal to 10.0 MPa. The result with SD of 0 MPa showed only two cracks, because stress reached up to 10 MPa twice. After that, softening behavior was observed. However, changing the standard deviation (SD) resulted in significant changes of the fracture process from strain softening to strain hardening, as shown in Fig. 16. From the physical point of view, initial crack occurs at weakest cross section, and second crack occurs at the next weakest cross section. Sequential cracking along specimen axis seems to be strongly affected by distribution of matrix strength. Regarding the numerical results, larger standard devia-

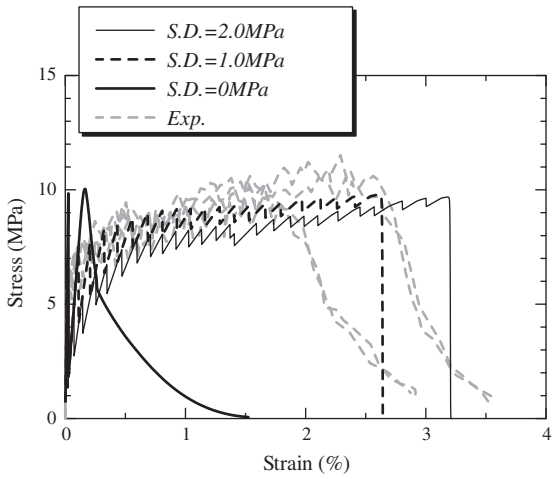

Fig. 16. Effect of nonuniform distribution of matrix strength (V_f = 1.5%).

tions of matrix strength produced higher strain capacities in the analyses, under the assumption of constant bridging strength of the fibers.

Fig. 17 shows averaged crack width during the fracture process in the case of 1.5% fiber volume fraction. The numerical model simulates steady state cracking behavior, which means no significant increase of crack width up to final fracture. This behavior is similar to the experimental trend [19], and the quantitative crack width simulation might be useful to access the transport property (e.g. water permeability) of SHCC [20].

Fig. 18 shows crack patterns in the case of 1.5% fiber volume fraction with SD = 1.0 MPa. Although the previous analysis (based on a uniform distribution of matrix strength) indicated constant crack spacing as shown in Fig. 14, the analysis considering the assumed probabilistic distribution of matrix strength shows nonuniform crack spacing.

Along with this probabilistic assignment of matrix strength, specimens with different fiber contents can be also simulated. Especially, the slight strain hardening shown in Fig. 19b was reproduced for the case of 1% fiber volume fraction, while the previous analysis exhibited softening behavior, as shown in Fig. 13b.

5.2. Effect of fiber distribution along specimen axis

In order to assess the effects of fiber distribution in the specimen, analysis was conducted by changing the coefficient of variation of number of fiber in each cross section, which corresponds to a potentially crack plane. In this model, each fiber is randomly positioned within the specimen, as shown in Fig. 20, and average number of cracks across each cross section was about 28,800, as tabulated in Table 2. Three kinds of analysis with different coefficient of variation of number of fibers in each cross section (COV = 0.0053, 0.054 and 0.11) were conducted. The matrix strength was equal to 7.5 MPa, and standard deviation (SD) was 1.0 MPa.

Fig. 21 shows the stress–strain relationship of specimens having different fiber distribution. The numerical results show that larger distribution of fiber having cross section with less fiber significantly reduces strain capacity.

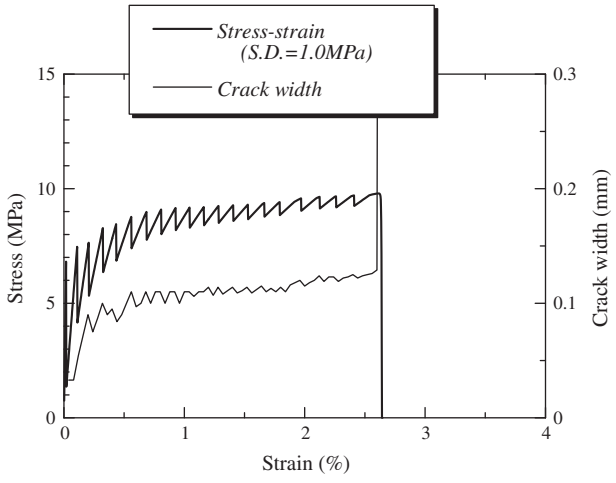

Fig. 17. Changing of crack width up to final failure (V_f = 1.5%).

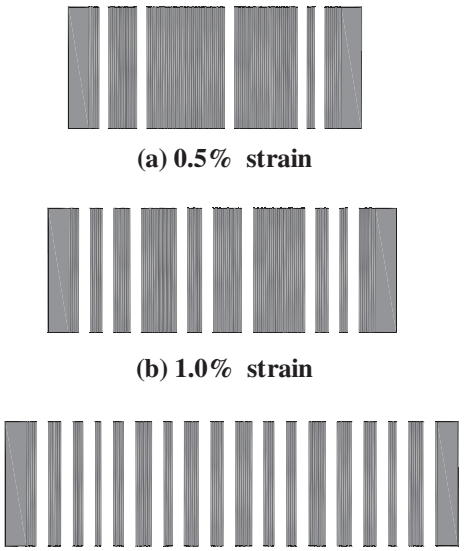

Fig. 18. Crack patterns of specimen considering nonuniform distribution of matrix strength (V_f = 1.5%).

6. Parametric study on specimen size

In this section, the effect of specimen size (length) on tensile response is conducted. There is a significant size effect on strength and tensile strain capacity in tension for the UHP-SHCC specimens [21,22].

Three specimen lengths and three specimen thicknesses were adopted with the same specimen width (30 mm), as shown in Table 3. Since element size along the specimen axis was constant (i.e. 1 mm), the number of elements for 50 mm and 200 mm gage lengths is half and twice that of the 100 mm case, respectively. Volume fraction of fiber is 1.5% for all cases. Besides the gage length, only the probabilistic distribution of matrix strength was considered in this parametric study. All other input parameters are the same as those of the previous analyses.

Fig. 22 shows the numerical results obtained for uniform matrix strength. Note that the fiber bridging strength is significantly higher than the matrix strength. Basically the number of stress drops corresponds to the number of cracks, and it depends on the number of elements (potential crack planes) along the specimen axis (i.e. longer specimens have a larger number of potential crack planes). Although strain capacity was decreased with the increasing of specimen length, the difference between the strain capacity of the 200 mm case and that of the 50 mm case was only 0.65%. Fig. 23 shows the numerical results for the assumed probabilistic distribution of matrix strength (the matrix strength is close to

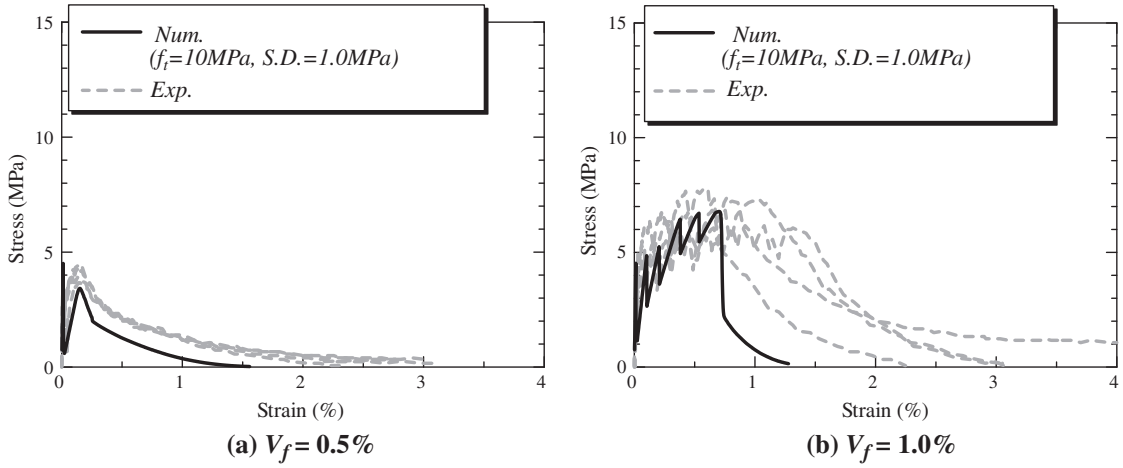

Fig. 19. Stress–strain curves considering nonuniform distribution of matrix strength.

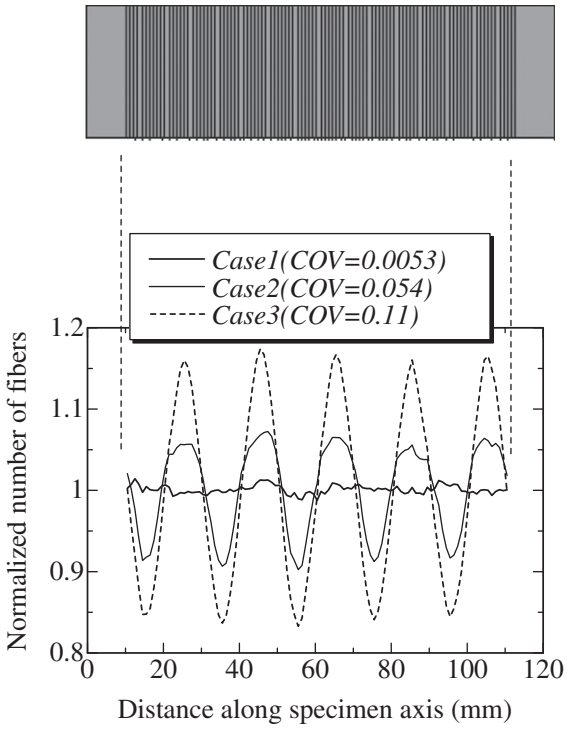

Fig. 20. Number of fibers along specimen axis.

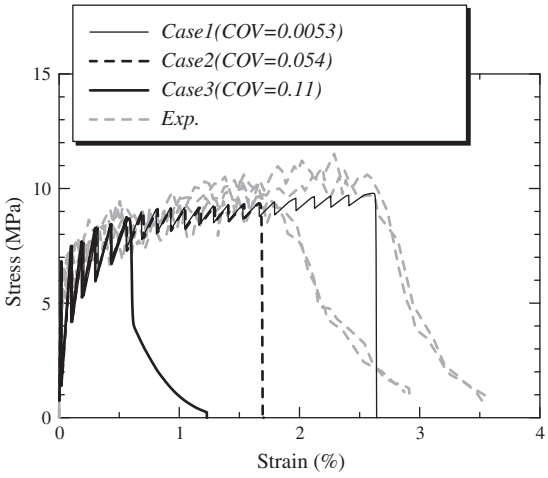

Fig. 21. Stress–stain curves of specimens with different fiber distribution (matrix: f_t = 10 MPa, SD = 1.0 MPa).

Table 2
Coefficient of variation of the number of fibers intersecting a potential cracking plane (average number of fiber: 28,800, V_f = 1.5%).

	Coefficient of variation
Case 1	0.0053
Case 2	0.054
Case 3	0.11

Table 3
Numerical analysis cases concerning specimen length and thickness.

Length	Thickness		
	6.5 mm	13 mm	26 mm
50 mm		X[a]	
100 mm	X	X[a]	X
200 mm		X[a]	

[a] Uniform strength cases were also analyzed for comparison.

the fiber bridging strength), and a decreased in strain capacity was also observed. The difference between the strain capacity of the 200 mm case and that of the 50 mm case was, however, more than 1.2%. This means that, for these analyses, the probabilistic distribution of matrix strength decreases the strain capacity to a greater degree with increasing specimen length. In SHCC materials, ultimate fracture (localization) depends on the crack with the lowest fiber bridging strength within the specimen. For longer specimens, there is increased probability of having a potential cracking plane with fewer fibers (due to the random nature of the procedure for introducing fibers within the model.) For greater variations in matrix strength about the mean strength value, a larger number of potential cracking planes are stronger than the fiber bridging strength at the localized crack. Because cracks do not form at these stronger locations prior to fracture localization, the strain capacity is reduced.

Fig. 24 presents stress–strain curves for specimen models with different thickness. It is observed that the strength and strain capacity of thinner specimens are increased. The thinner specimen induces greater alignment of the fibers in the loading direction,

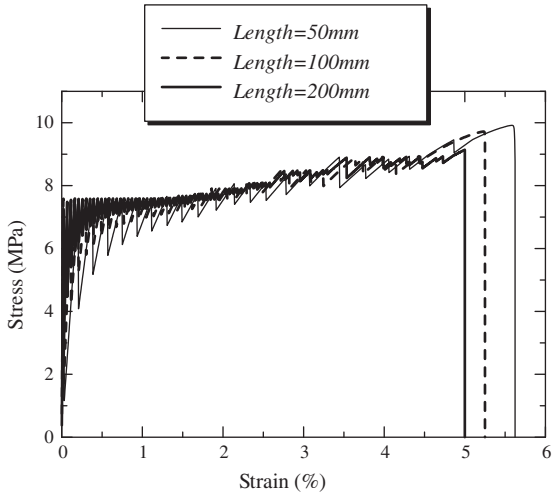

Fig. 22. Stress–stain curves of specimens with different specimen length (matrix: f_t = 7.5 MPa, no probability distribution of matrix strength).

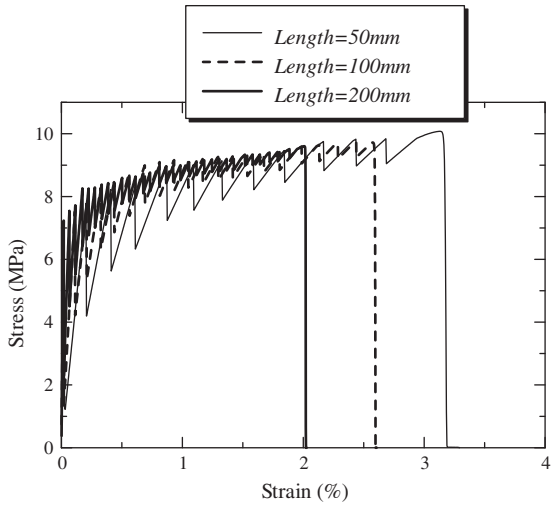

Fig. 23. Stress–stain curves of specimens with different specimen length (matrix: f_t = 10 MPa, SD = 1.0 MPa).

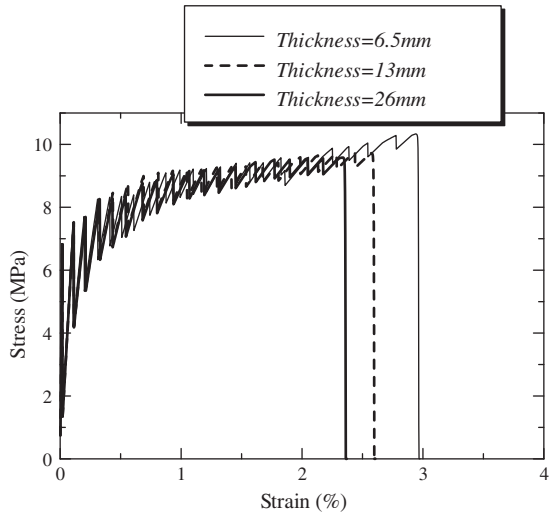

Fig. 24. Stress–stain curves of specimens with different specimen thickness (matrix: f_t = 10 MPa, SD = 1.0 MPa).

which would increase the nominal fiber bridging strength at potential cracking planes.

7. Conclusions

This paper has introduced a numerical model for three-dimensional analysis of SHCC fracture, in which the salient features of the material meso-scale (i.e. matrix, short fibers and their interface) are discretized. The model capabilities were assessed through analyses of Ultra High Performance-Strain Hardening Cementitious Composites (UHP-SHCC). The findings obtained include the following:

(1) With a reference to a material characterized by high tensile strength and strain hardening behavior with multiple fine cracks in tension (UHP-SHCC), this model roughly simulated mechanical response represented by stress–strain curves and crack pattern.
(2) Probabilistic parametric analyses were performed to interpret fracture mechanisms of strain hardening and multiple fine cracks in UHP-SHCC. Strain capacity was increased due to larger distribution of matrix strength, when the fiber bridging strength is higher than the average matrix strength. Strain capacity is mainly decreased with increasing of heterogeneity due to fiber distribution, when the fiber bridging strength is higher than the average matrix strength. When the fiber bridging strength is close to the average matrix strength, the variation of matrix strength also affects the strain capacity.
(3) Probability distribution of each material property, such as matrix strength and fiber distribution, was essential to estimate the fracture process of SHCC type materials.
(4) Analysis concerning difference of both specimen length and thickness, in which probability distribution of matrix strength was considered, indicated the mechanism of strain capacity in tension. Longer specimen provided less strain capacity comparing that in shorter one, and thinner specimen exhibited higher strain capacity comparing that of thicker specimen.

Acknowledgment

The authors would like to thank Mr. Kunihiro Kozawa, who was a graduate student of Nagoya University, for his important contributions to this research work.

References

[1] Li VC. From micromechanics to structural engineering – the design of cementitious composites for civil engineering applications. J Struct Mech Earthq Eng, JSCE 1993;10(2):37s–48s.
[2] Han TS, Feenstra PH, Billington SL. Simulation of highly ductile fiber-reinforced cement-based composite components under cyclic loading. ACI Struct J 2003;100(6):749–57.
[3] Suwada H, Fukuyama H. Nonlinear finite element analysis on shear failure of structural elements using high performance fiber reinforced cement composite. J Adv Concr Technol 2006;4(1):45–57.
[4] Fischer G, Stang H, Dick-Nielsen L. Initiation and development of cracking in ECC materials: experimental observations and modeling, fracture mechanics of concrete and concrete structures. In: Proc of FRAMCOS6; 2007. p. 1517–22.
[5] Maalej M. Tensile properties of short fiber composites with fiber strength distribution. J Mater Sci 2001;36:2203–12.
[6] Bolander JE, Saito S. Discrete modeling of short-fiber reinforcement in cementitious composites. Adv Cem Based Mater 1997;6:569–91.
[7] Jun P, Mechtcherine V. Behaviour of strain-hardening cement-based composites (SHCC) under monotonic and cyclic tensile loading: Part 2 Modelling. Cem Concr Compos 2010;32(10):810–8.
[8] Kabele P. New developments in analytical modeling of mechanical behavior of ECC. J Adv Concr Technol 2003;1(3):253–64.

[9] Berton S, Bolander JE. Crack band modeling of fracture in irregular lattices. Comput Methods Appl Mech Eng 2006;195:7172–81.
[10] Thomure J, Bolander JE, Kunieda M. Reducing mesh bias on fracture within rigid-body spring networks. J Struct Mech Earthq Eng, JSCE 2001;682/I-56:15–23.
[11] Cox H. The elasticity and strength of paper and other fibrous materials. Brit J Appl Phys 1952;3.
[12] Kunieda M, Kozawa K, Ueda N, Nakamura H, Ogura H. Three-dimensional meso-scale analysis for strain hardening cementitious composites, creep, shrinkage and durability mechanics of concrete and concrete structures. In: Proc of CONCREEP8; 2008. p. 745–51.
[13] Kozawa K, Kunieda M, Kanda T, Nakamura H. Bond properties of synthetic fiber embedded in ultra high strength matrix. In: Proceedings of the Japan concrete institute, vol. 30(1); 2008. p. 231–36 [in Japanese].
[14] Li VC, Wang Y, Backer S. Effect of inclining angle, bundling, and surface treatment on synthetic fiber pull-out from a cement matrix. Composites 1990;21(2):132–40.
[15] Kozawa K. Study on tensile fracture mechanism of ultra high performance-strain hardening cementitious composites and its modeling. Master thesis of Nagoya University; 2008 [in Japanese].
[16] Kanda T, Li VC. Interface property and apparent strength of high-strength hydrophilic fiber in cement matrix. J Mater Civil Eng, ASCE 1998;10(1):5–13.
[17] Kunieda M, Denarié E, Brühwiler E, Nakamura H. Challenges for strain hardening cementitious composites – deformability versus matrix density. In: Proc of the fifth international RILEM workshop on HPFRCC; 2007. p. 31–8.
[18] Kamal A, Kunieda M, Ueda N, Nakamura H. Evaluation of crack opening performance of a repair material with strain hardening behavior. Cem Concr Compos 2008;30(10):863–71.
[19] Li VC. On engineered cementitious composites (ECC) – a review of the material and its applications. J Adv Concr Technol 2003;1(3):215–30.
[20] Lepech MD, Li VC. Water permeability of engineered cementitious composites. Cem Concr Compos 2009;31(10):744–53.
[21] Kunieda M, Hussein M, Ueda N, Nakamura H. Enhancement of crack distribution of UHP-SHCC under axial tension using steel reinforcement. J Adv Concr Technol 2010;8(1):49–57.
[22] Kanakubo T. Tensile characteristics evaluation method for ductile fiber-reinforced cementitious composite. J Adv Concr Technol 2006;4(1):3–17.